Chemical effect on the structural and dynamical properties in Zr-Ni-Al liquids

H. L. Peng,[1,2,*] F. Yang,[2] S. T. Liu,[2] D. Holland-Moritz,[2] T. Kordel,[2] T. Hansen,[3] and Th. Voigtmann[2,4,†]
[1]*School of Materials Science and Engineering, Central South University, 932 South Lushan Rd, 410083 Changsha, China*
[2]*Institut für Materialphysik im Weltraum, Deutsches Zentrum für Luft- und Raumfahrt (DLR), 51170 Köln, Germany*
[3]*Institut Laue-Langevin (ILL), 38042 Grenoble, France*
[4]*Department of Physics, Heinrich-Heine-Universität Düsseldorf, Universitätsstraße 1, 40225 Düsseldorf, Germany*

(Received 4 April 2019; revised manuscript received 26 June 2019; published 11 September 2019)

We develop an embedded-atom method (EAM) model to perform classical molecular-dynamics computer simulations of a model of Zr-Ni-Al ternary melts, based on the existing binary ones. The EAM potential is validated against a broad range of experimental data for the liquid melt, including both static-structure factors and dynamical data on the mass-transport coefficients. We use our simulation model to address the structural and dynamical changes induced by a systematic replacement of Zr by Al in $Zr_{75-x}Ni_{25}Al_x$ ($x = 0$–30) ternary alloys. We find strong chemical-ordering effects exhibited as the locally preferred structure when the Al-concentration c_{Al} is increased. Along with the chemical effects, effective-power-law relations are found between the self-diffusion coefficients in the melts, with an exponent that monotonically decreases with increasing Al concentration. The associated Stokes-Einstein relation between diffusivity and viscosity breaks down at higher temperature upon Al addition. We also address the influence of Al admixture on the vibrational spectrum of the melt. With increasing c_{Al}, sound waves move faster, and an optical vibrational mode is found.

DOI: 10.1103/PhysRevB.100.104202

I. INTRODUCTION

When manufacturing metallic materials of amorphous structure by melting several metallic elements together, numerous factors related to the chemical composition influence the materials properties of the resulting compounds [1]. To understand the generic physical principles behind such mixing effects, it is often helpful to distinguish "entropic" mixing contributions, i.e., those attributable predominantly to the difference in atomic sizes, from those that are induced by the specifics of the interatomic interactions (and that we subsume as "chemical effects" in the following).

Metallic glasses are an example where entropic effects serve as a particularly useful reference to discuss dynamical features, in particular the mass-transport mechanisms as exhibited through the transport coefficients (self-diffusion and viscosity most prominently). These effects are elucidated by the hard-sphere model of atoms; an analogy that has been proposed already in the 1960s [2,3]. In the hard-sphere model, a suitable set of empirical atomic radii is used to map the metallic melt onto a mixture of hard spheres of different sizes. At a given composition, the effective packing density (packing fraction) of the hard-sphere mixture is then the only relevant parameter, and indeed it correlates well with, for example, the temperature and sometimes system dependence of viscosity or diffusion coefficients [4–6].

An indicator of nonentropic mixing effects is a composition-dependent atomic radius of the hard-sphere mapping, as it has been reported for Zr atoms in Cu-Zr and Ni-Zr glasses [7], and in Co-Sn alloys [8] based on x-ray diffraction experiments and computer simulation. Even if the generic dynamical behavior of the melt (such as the temperature dependence of transport coefficients) may still be captured by the hard-sphere analogy, some aspects that are in particular relevant for the mixing behavior and the composition-dependent material properties differ significantly. The ratios of mass-transport coefficients associated to the different species, which show strong nonentropic coupling, e.g., in Zr-Ni [9,10] or Nb-Ni [11], provide an example. A prominent system class featuring strong deviations from purely entropic effects is that of melts containing Al, such as Al-Fe [12], Al-Au [13], Al-Ni [14,15], Zr-Cu-Al [16], or Zr-Co(Ni)-Al [17].

Although not uniquely nonentropic, anomalous temperature behavior is often found in the mass-transport coefficients such as viscosity, η, or self-diffusion of a select species, D. In its extent, one can argue, they are indicative of strong chemical effects. An Arrhenius to super-Arrhenius transition has been reported for Cu-Zr [18,19] and Zr-Cu-Al liquids [20] in computer simulation, as well as for Al-Cu [21] and Zr-Cu-Ni-Al [22] in experiments. Associated with this is a violation of the empirical Stokes-Einstein (SE) relation, $D\eta \propto T$, that is found to hold in many liquids. Usually, this transition and the violation of the SE relation are found near or a little above the mode-coupling crossover temperature, T_c, but much lower than the liquidus temperature. In the above examples, the deviations set in at much higher temperatures, indicating strong chemical effects from the outset. They have been linked to the emergence of "dynamical heterogeneities" for example in AuSi melts [23], thus connecting to a concept that is often invoked to rationalize the slow relaxation behavior of glass-forming fluids. In Zr-Ni liquids, the relation $D(T)\eta(T) \approx$

---

[*] hailong.peng@csu.edu.cn

[†] thomas.voigtmann@dlr.de

const (instead of the linear temperature dependence suggested by the SE relation) was found in a wide temperature range up to 500 K above the liquidus temperatures [24]. This was interpreted as a sign of transport mechanisms that couple collective relaxation and the self-diffusivity of both species much more strongly than is expected on entropic grounds, or more generally for the simple-liquid state [25].

One expects in general that the observed dynamical features can be traced back in origin to peculiarities of the static structure of the melt. The above results highlight that for many alloys, in particular Al-containing ones, chemical effects cannot be neglected in this description. A prominent structural indicator of chemical short-range order (CSRO) as a prototypical nonentropic contribution is often a prepeak in the partial static structure factors [9,12,13,15,26], even if such prepeaks might be masked in the experimentally accessible total scattering signal.

To account for the sluggish dynamics in melts and glass-forming liquids, a variety of structural indicators (including CSRO, but also icosahedral short-range order, local fivefold symmetry, structural entropy, and structural fragility) [27–33] has been proposed. Little focus however has been given to the evolution of atomic-packing mechanisms in the alloys as their composition is changed systematically. In particular for the change of Al concentration, we have recently found a contraction of the effective size of Al atoms in Al-Au binary alloys: the nearest-neighbor atomic interaction distance of these atoms exhibits a strong concentration dependence, i.e., a dependence on the chemical environment [13]. While these findings point to the relevance of structural changes induced by Al, it remains unclear if this strong influence can also describe the behavior seen in multicomponent alloys, or if Al is not the majority component. Furthermore, these local changes are often difficult to assess in experiment, because they manifest themselves primarily in the atomic-species-resolved pair structure, that is, for example, unfeasible to obtain from scattering experiments in alloys with three or more constituents.

Molecular dynamics (MD) simulation is a useful tool to gain insight into the dynamics of liquids on an atomic level, as it accesses both the relevant time and length scales for the melt dynamics. However, the reliability of such classical simulation results depends on the judicious choice of empirical interatomic potentials, especially for a system where the specific chemical potential between different atomic species is of great importance. Originally, semiempirical interatomic potentials are mostly developed based on solid state properties, e.g., by parametrizing the force field obtained by *ab initio* quantum simulation in crystals, to match the crystalline properties measured in experiment (for instance, lattice constant and moduli). More recently, development of the effective interatomic potential includes information for amorphous states, e.g., the static structure factors in liquids or glasses, for instances of describing pure elements [34–36] and binary alloys [37–39]. The optimization of an empirical potential for these properties, however, does not guarantee a good representation of the dynamic behavior in the liquid state, because there, different properties of the true free energy can become important. Training for the dynamic properties of the liquid state (i.e., adaptation of the empirical parameters to known melt properties such as viscosity or diffusivity) is often required for a good performance of the empirical potential on the liquid dynamics [13,40]. Due to the lack of reliable experimental data in the melt, this is usually difficult.

In this work, we develop an interatomic potential in the form of the embedded-atom method (EAM) for Zr-Ni-Al liquids based on existing works for the related binary compounds [16,38,41]. We gauge this potential against accurate experimental thermodynamic and dynamical quantities, including the mass density, a set of total and partial static structure factors, shear viscosity and self-diffusion measurements. We have, to this end, obtained experimental data by use of containerless processing techniques combined with quasielastic neutron scattering, in order to provide measurements with a much higher reliability and accuracy as previously available.

Although there exist already EAM potentials for this ternary system [42–44], careful validation of these potentials on the structural and dynamical aspects was still absent. We demonstrate that our newly developed EAM potential, gauged against new and accurate experimental data in the melt, provides a good overall description of the known experimentally determined structure-dynamics properties of Zr-Ni-Al liquid alloys. We then use this potential in MD simulations to investigate the effects of strong chemical interaction as introduced by admixture of Al, by systematic replacement of Zr with Al. Here our focus is on the change in local order as expressed in the species-resolved partial static structure factors. We thus provide a new structural model for the Zr-Ni-Al alloy that connects to previous investigations of chemical short-range order in the related binary systems, where significant prepeaks in the partial static structure factors have been found (e.g., in Zr-Ni [9] and Ni-Al liquids [14,15]). These structural effects are linked to certain dynamical properties such as the mass transport that shows strong coupling between the species (as previously reported for Zr-Ni liquids [24]), and a composition-dependent self-diffusivity (previously known for Ni-Al liquids [15,45]) that shows strong differences between the species.

The paper is organized as follows: details on how the interatomic potential is constructed are provided, and the applied experimental measurement methods are described in Sec. II. Experimental data and the validation of the developed EAM potential in Ni-Al, Zr-Ni, and Zr-Ni-Al liquids are presented in Sec. III. A systematic investigation on the structural and dynamical properties in $\mathrm{Zr}_{75-x}\mathrm{Ni}_{25}\mathrm{Al}_x$ ($x = 0, 5, 15, 20, 25, 30$) liquids by computer simulation is conducted in Sec. IV. Finally, we conclude in Sec. V.

II. METHODS

A. Potential development

A popular class of semiempirical potentials used in classical MD simulations of metallic alloys are the embedded atom method (EAM) [46] and the Finnis-Sinclair (FS) potentials [47]. For a multicomponent system, the EAM requires to specify the potential of the pure elements, and one cross term for every pair of distinct atomic species, while the FS potential requires two cross terms for the electronic density for every distinct-species pair. The total energy in the EAM is written as

$$E_{\text{tot}} = \sum_i F_\alpha^i(\rho_i) + \frac{1}{2}\sum_{i\neq j}\phi_{\alpha\beta}(r_{ij}), \tag{1}$$

where the embedding energy F is a function of the atomic electron density ρ, ϕ is a pair potential interaction, α and β are the element types of atoms i and j, and r_{ij} is the distance between these two atoms. In the FS potential scheme, the electron density at atom i is calculated as $\rho_i = \sum_{j\neq i} f_{\alpha\beta}(r_{ij})$, where $f_{\alpha\beta}(r)$ designates the electron density generated by element type β at distance r from a central atom of type α. The functions $\phi_{\alpha\beta}(r)$ and $f_{\alpha\beta}(r)$ usually are the results of empirical modeling based on available *ab initio* data.

An interatomic potential for the ternary Zr-Ni-Al system includes three pair interactions, i.e., the Zr-Ni, Ni-Al and Zr-Al pairs. For the Zr-Ni pair, we have based our model on the semiempirical potential developed by Mendelev *et al.* [37,38], which is known to provide a good description of the Zr-Ni metallic glass and the properties of its liquid state. For the Ni-Al pairs, we employ the potential developed by Mishin *et al.* [41], which captures well the diffusion and interdiffusion behavior in this binary system [40]. For the Zr-Al pairs, the potential functions partially come from Mendelev and Mishin, while the pair-potential term ϕ is taken from from a potential developed by Cheng [16] to describe Zr-Cu-Al metallic glasses.

To allow for a meaningful combination of these different potential contributions, the electronic densities are first normalized. Consider the transform $\rho(r) \to \rho(r)/\rho_s$, and $F(\rho) \to F(\rho/\rho_s)$. This leaves invariant any of the individual-species EAM potential but changes the performance of the combined EAM potential including cross terms. In order to make the electronic density contributions reasonably comparable among the different potentials taken from the sources mentioned above, the parameter ρ_s is chosen such that $\rho_{\text{NiNi}}(r = 2.5\,\text{Å})$ is equal to unity both for Mendelev's and Mishin's potential. This transformation causes the electron density function $\rho_{\text{NiNi}}(r)$ to mostly collapse for these two different interatomic potentials, in the distance range from $r = 2.0\,\text{Å}$ to the force cutoff. Another invariant transformation for the individual EAM potential can be conducted on the embedding function term, i.e., $F(\rho) \to F(\rho) + k\rho$, and $\phi(r) \to \phi(r) - 2k\rho(r)$ [48]. Testing the parameter k in a reasonable range gives no improvement on the potential performance. Thus, we do not incorporate this parameter in our model.

After the electronic density normalization, an empirical scaling is applied both to the distance and the potential amplitude in order to improve the predictions in the liquid state [13,26,40,49], i.e., $\rho(r) \to \rho(r/r_s)$, $\phi(r) \to \phi(r/r_s)$, and $F(\rho) \to \lambda F(\rho)$, $\phi(r) \to \lambda\phi(r)$. The role of the scale factor r_s is mainly to change the mass density of the system, while λ modulates the dynamic behavior of the system. In broad terms, $r_s < 1$ will dilute the system, while $\lambda > 1$ jams the system leading to a decrease of atomic mobility for the corresponding element, and vice versa. The scaling parameters for the individual atomic species are tuned against known pure-element properties, while the scaling parameters entering the distinct-species interactions are tuned mainly against known experimental data for the corresponding binary alloys. For instance, the parameters r_s^{Al} and λ^{Al} are adjusted according to the experimental data of pure Al liquid, with the same procedure as in Ref. [13]. The full set of parameters was optimized in order to provide best overall agreement with the available experimental data, as will be detailed below. The values of these parameters are listed in Table I. Note that in principle, the rescaling procedure is not guaranteed to provide an optimal EAM potential, because the functional form of the original binary potentials is not modified. Our procedure provides a simple and reasonable way to adjust existing EAM potentials from the solid to the liquid state.

TABLE I. List of scaling parameters applied in the Zr-Ni-Al EAM potential used in this work (see text).

Mishin potential	r_s^{Ni}	r_s^{Al}	$r_s^{\text{Ni-Al}}$	λ_{Ni}	λ_{Al}	$\lambda_{\text{Ni-Al}}$
	0.99	0.99	0.95	0.75	0.713	0.6
Mendelev potential	r_s^{Ni}	r_s^{Zr}	$r_s^{\text{Ni-Zr}}$	λ_{Ni}	λ_{Zr}	$\lambda_{\text{Ni-Zr}}$
	1	1	1	1.05	1.2	1.1
Others	$r_s^{\text{Zr-Al}}$	$\lambda_{\text{Zr-Al}}$	α			
	0.95	0.7	0.84			

After the normalization and scaling of the electron densities, we combine these terms by introducing one additional parameter α ($0 \leqslant \alpha \leqslant 1$), which weighs the contribution of the Ni-Ni interaction from Mendelev's potential (value also listed in Table I). In summary, the embedding energy function F, electron density function f, and pair potential interaction function ϕ for ternary Zr-Ni-Al alloys are specified as

$$\begin{aligned}
F_{\text{Zr}}(\rho) &= F_{\text{Zr}}^{\text{Men}}(\rho),\\
F_{\text{Ni}}(\rho) &= F_{\text{Ni}}^{\text{Men}}(\rho)\alpha + F_{\text{Ni}}^{\text{Mi}}(\rho)(1-\alpha),\\
F_{\text{Al}}(\rho) &= F_{\text{Al}}^{\text{Mi}}(\rho)
\end{aligned}$$

for the embedding energy,

$$\begin{aligned}
f_{\text{ZrZr}}(r) &= f_{\text{ZrZr}}^{\text{Men}}(r),\\
f_{\text{ZrNi}}(r) &= f_{\text{ZrNi}}^{\text{Men}}(r),\\
f_{\text{ZrAl}}(r) &= \big[f_{\text{ZrZr}}^{\text{Men}}(r) + f_{\text{AlAl}}^{\text{Mi}}(r)\big]/2,\\
f_{\text{NiZr}}(r) &= f_{\text{NiZr}}^{\text{Men}}(r),\\
f_{\text{NiNi}}(r) &= f_{\text{NiNi}}^{\text{Men}}(r)\alpha + f_{\text{NiNi}}^{\text{Mi}}(r)(1-\alpha),\\
f_{\text{NiAl}}(r) &= \big[f_{\text{NiNi}}(r) + f_{\text{AlAl}}^{\text{Mi}}(r)\big]/2,\\
f_{\text{AlZr}}(r) &= f_{\text{ZrAl}}(r),\\
f_{\text{AlNi}}(r) &= f_{\text{NiAl}}(r),\\
f_{\text{AlAl}}(r) &= f_{\text{AlAl}}^{\text{Mi}}(r),
\end{aligned}$$

for the electron densities, and

$$\begin{aligned}
\phi_{\text{ZrZr}}(r) &= \phi_{\text{ZrZr}}^{\text{Men}}(r),\\
\phi_{\text{NiZr}}(r) &= \phi_{\text{NiZr}}^{\text{Men}}(r),\\
\phi_{\text{NiNi}}(r) &= \phi_{\text{NiNi}}^{\text{Men}}(r)\alpha + \phi_{\text{NiNi}}^{\text{Mi}}(r)(1-\alpha),\\
\phi_{\text{AlZr}}(r) &= \phi_{\text{AlZr}}^{\text{Cheng}}(r),\\
\phi_{\text{AlNi}}(r) &= \phi_{\text{AlNi}}^{\text{Mi}}(r),\\
\phi_{\text{AlAl}}(r) &= \phi_{\text{AlAl}}^{\text{Mi}}(r)
\end{aligned}$$

for the direct pair potentials. Here, the superscripts indicate the scaled EAM functions from the different sources: Min for Mishin [41], Men from Mendelev [38], and Cheng from Cheng [16].

MD simulations were performed with $N = 3000$ atoms with periodic boundary conditions, using the software package LAMMPS [50]. The equations of motion were integrated with a standard velocity-Verlet algorithm and a time step of 1 fs at high temperatures ($T \geqslant 1600\,\mathrm{K}$), and 2 fs otherwise. Each simulation run was first equilibrated at 2200 K and subsequently cooled to the desired temperature in the NPT ensemble (constant particle number, zero external pressure, and linearly decreasing temperature). After short-time relaxation, production runs are performed in the microcanonical ensemble (NVE), where the total energy and temperature are monitored to show no noticeable drift. We have simulated up to 10^6 time steps at low temperature, which is at least one order of magnitude longer than the decay time of typical dynamic correlation functions. At every composition and temperature investigated, an average over 10 different samples was used to improve statistics.

The viscosity of the simulated alloy is calculated via the standard Green-Kubo relation, $\eta = V/k_BT \int_0^\infty \langle P_{xy}(t)P_{xy}(0)\rangle\, dt$, where P_{xy} are the off-diagonal elements of the microscopic stress tensor and V is the volume of the simulated cubic box. The diffusivity of atomic type α is obtained from the mean-squared displacement via the Einstein relation: $D_\alpha = \lim_{t\to\infty}\langle|\mathbf{r}_i^\alpha(t) - \mathbf{r}_i^\alpha(0)|^2\rangle/6t$. Since our system is isotropic, the partial static structure factors of the multicomponent alloys are related to the Fourier transformation of the radial distribution functions by

$$S_{\alpha\beta}(q) = \delta_{\alpha\beta} + \frac{\sqrt{N_\alpha N_\beta}}{V}\int_V 4\pi r^2[g_{\alpha\beta}(r) - 1]\frac{\sin(qr)}{qr}\, dr, \tag{2}$$

where N_α and N_β are the number of atoms of type α and β, and $g_{\alpha\beta}(r)$ are the partial pair correlation functions. In order to compare with experimental results, static structure factors are converted into Faber-Ziman structure factors by

$$S_{\alpha\beta}^{\mathrm{FZ}}(q) = (S_{\alpha\beta}(q) - \delta_{\alpha\beta})/\sqrt{c_\alpha c_\beta} + 1, \tag{3}$$

where $c_\alpha = N_\alpha/N$ is the number concentration of species α. For the ternary system, we also compare with the total static structure factor obtained from neutron scattering,

$$S(q) = \frac{\sum_{\alpha,\beta} c_\alpha c_\beta b_\alpha b_\beta S_{\alpha\beta}^{\mathrm{FZ}}(q)}{\sum_{\alpha,\beta} c_\alpha c_\beta b_\alpha b_\beta}, \tag{4}$$

where the b_α are the scattering lengths of atomic type α [whose value depends on the scattering experiment that is performed to obtain $S(q)$].

B. Experimental measurement

Ternary $Zr_{70}Ni_{25}Al_5$ and $Zr_{60}Ni_{25}Al_{15}$ samples were prepared by arc-melting the appropriate fractions of pure Zr (99.97%, smart-elements), Ni (99.995%, Alfa Aesar), and Al (99.9999%, Hydro Aluminum) together under a Ti-gettered high-purity argon (99.9999%) atmosphere. For the neutron diffraction experiments samples with masses of about 400–500 mg were prepared. For viscosity and density measurements master alloys of about 1 g were cast into rods of 1.5 mm in diameter. Fractions of the rods of about 50–80 mg were then remolten into small spheres. The deviations from the nominal sample compositions are below 0.5 at%, as verified by energy-dispersive x-ray spectroscopy.

Due to the high chemical reactivity of the melts at elevated temperatures, all measurements were performed containerlessly in an electrostatic levitator. This further allows to access the metastable state of an undercooled liquid since heterogeneous nucleation is suppressed. The levitated sample was heated and molten by diode lasers with a wavelength of 808 nm under high vacuum conditions ($<10^{-6}$ mbar). The sample temperatures were measured by single-color pyrometry, calibrated at the liquidus temperature of the alloy ($T_{\mathrm{L,Zr_{60}Ni_{25}Al_{15}}} = 1215$ K, measured by differential thermal analysis) assuming a temperature-independent liquid emissivity. The uncertainty in the measured temperatures is estimated to be ±10 K, taking into account of the uncertainties in the liquid emissivity, the liquidus temperature, and the temperature gradient in the sample.

For measuring the liquid viscosity on a levitated droplet the oscillating drop method was utilized [51]. To induce surface oscillations of the liquid droplet a sinusoidal oscillation voltage was superimposed onto the levitation voltage. The decay of the oscillation amplitude after switching off the excitation (oscillation voltage) was then recorded with a high speed video camera at a frame rate of 2000 Hz. The liquid viscosity can be derived from the characteristic decay time and the oscillation mode assuming pure internal friction [52]. Only dipole mode oscillations in the vertical direction of the droplet was used for calculating the liquid viscosity. The choice of a relatively small sample mass below 100 mg reduces possible measurement artifacts such as additional surface oscillations and fluid flow [53]. The density of the melt was obtained via video diagnostics during cooling of the sample. The projected area of the back-lit sample was recorded by a high-speed camera and then derived by integrating the edge of the sample shadow fitted by a sum of Legendre polynome up to the sixth order. The sample volume can be calculated correspondingly assuming rotation symmetry around the droplet normal to the projection direction. The density is obtained from the volume and the mass of the sample.

For the structural study on liquid $Zr_{70}Ni_{25}Al_5$ and $Zr_{60}Ni_{25}Al_{15}$ neutron diffraction experiments were performed on the high-flux diffractometer D20 at the Insitut Laue-Langevin [54]. Samples were processed in an electrostatic levitator specially designed for neutron scattering experiments [55]. A wavelength of 0.94 Å was chosen, which is a compromise between the neutron flux and the accessible range of momentum transfer q, and q resolution. Details of the experimental setup are given in Refs. [55–57]. The neutron data reduction procedure including background subtraction, self-absorption correction, normalization to vanadium standards, and multiple and magnetic scattering corrections is described in Ref. [58]. The total structure factor of molten $Zr_{60}Ni_{25}Al_{15}$ was obtained at five different temperature between 1042 K (undercooled by more than 170 K) and 1354 K (about 140 K above T_L). The structure factor of the $Zr_{70}Ni_{25}Al_5$ alloy was measured at 1300 K.

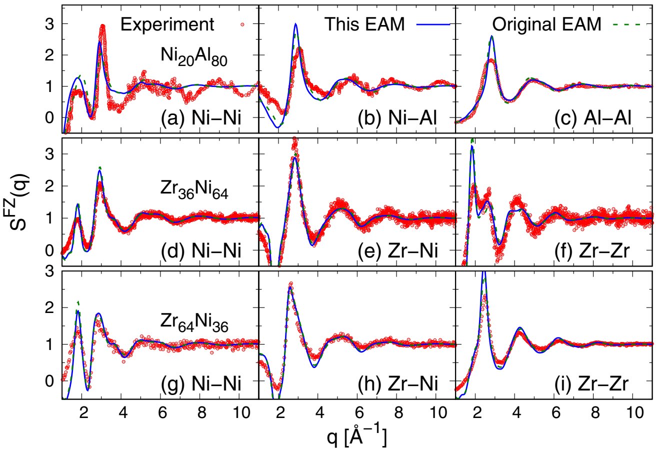

FIG. 1. Faber Ziman static structure factors for liquid binary mixtures at 1300 K: (a)–(c) for $Ni_{20}Al_{80}$, (d)–(f) for $Zr_{36}Ni_{64}$, and (g)–(i) for $Zr_{64}Ni_{36}$. Red circles represent experimental data [(a)–(c): from Ref. [14]; (d)–(f): from Ref. [10]; (g)–(i): from Ref. [59]]. Solid blue lines are results of our MD simulations, and the dashed green lines are results of MD simulations using the original EAM potentials developed in Refs. [41] and [38].

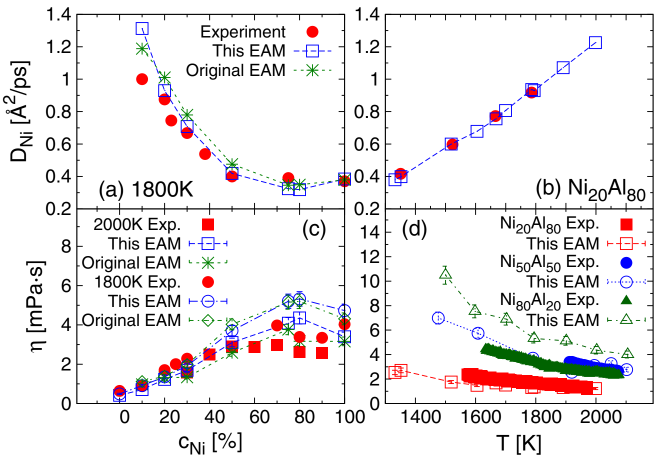

FIG. 2. Comparison of simulated values of D and η with experimentally determined data for Ni-Al liquids. Filled symbols are experimental data, open symbols results from our EAM potential, and star and diamond symbols are results from the original EAM potential [41]. (a) Concentration-dependent diffusion coefficient D_{Ni}, experimental data from Ref. [45]; (b) temperature dependence, data from Ref. [40]. (c)–(d) Concentration-dependent and temperature-dependent viscosity η, data from Ref. [60].

III. POTENTIAL VALIDATION

A. Binary mixtures

The scaling method that was conducted during the potential adjustment can in principle deteriorate the performance of the original potentials. To check that these effects are sufficiently small, we compare the partial static structure factors in the binary Ni-Al and Zr-Ni melts between simulation and experiment in Fig. 1. The value of the combination factor $\alpha = 0.84$ indicates that the major part of the contribution on Ni-Ni interactions comes from Mendelev's potential (which is developed for Zr-Ni alloys). However, this highly biased weight also performs well for Ni-Al alloys. The combined potential performs equally well as the original one in terms of the static structure [see Figs. 1(a)–1(c)] . The $S(q)$ measured by neutron scattering shows that there is a pronounced chemical short-range order in molten $Ni_{20}Al_{80}$ alloys [14,15]. This order is characterized by a prepeak in the partial static structure factors. Both the modified EAM potential and the original one can precisely reproduce the prepeak position but with the amplitude overestimated to some extent, as seen in Fig. 1(a).

As expected from the large value of α, our EAM potential is consistent with the original one in describing the static structure of Zr-Ni melts. All the peak positions as well as the peak amplitudes are well reproduced by these potentials both for $Zr_{36}Ni_{64}$ and $Zr_{64}Ni_{36}$ [except for some overestimation of the amplitude of the first peak for the Zr-Zr pairs; see Figs. 1(d)–1(i)]. Similar to the situation in liquid $Ni_{20}Al_{80}$, also here the prepeaks for Ni-Ni pairs indicate the chemical order in Zr-Ni liquids. Our simulation can precisely reproduce the prepeak positions, but slightly overestimates the amplitudes.

To provide an accurate description of the dynamic properties in the liquid state is one of the main purposes for the potential adjustment performed in this work. These properties are mainly affected by the tuning parameters λ. By adjustment of these parameters, the agreement of the simulation results with the diffusion coefficients D_{Ni} and the viscosity η available from experiment is improved: The concentration and temperature dependence of these transport coefficients are compared in Fig. 2 with the experimental results. For the diffusion coefficient D_{Ni}, the EAM potential performs almost as good as the original one, both regarding the concentration and the temperature dependence. For the viscosity η, our potential is consistent with experimental results for the Al-rich compositions, as shown in Fig. 2(c). But when the Ni concentration is more than 0.6, more significant discrepancies arise, and the MD results systematically overestimate η. Although our rescaling incorporates a reduction of the interatomic potential (as the scaling parameters λ for the Ni-Al mixture are all less than unity), the modified potential still predicts slower structural relaxation than observed in experiments. The experimental data indicate a maximum of η at $c_{\mathrm{Ni}} \approx 0.7$. The MD simulation qualitatively reproduces this behavior. Interestingly, a similar maximum of η has also been found in other binary Al-containing alloys, e.g., Al-Cu [61], and more significantly almost at the same Al-concentration point (i.e., $c_{\mathrm{Al}} \approx 0.3$). Utilizing the atomic-interaction size proposed by Miracle [62], the atomic size ratios are about 1.12 for these binary alloys. In the model of a binary mixture of hard spheres, the efficiency of the dense packing shows a maximum at a concentration of small particles of 0.7–0.8 when the size ratio is larger than 1.1 [63], coinciding with the composition of the maximum found for η in these binary mixtures (taking Al as big particle). Thus, the sluggish structural relaxation at the composition $c_{\mathrm{Al}} \approx 0.3$ can be qualitatively interpreted in terms of the hard-sphere model.

A similar comparison of the MD results with experiments has also been made for binary Zr-Ni mixtures. The

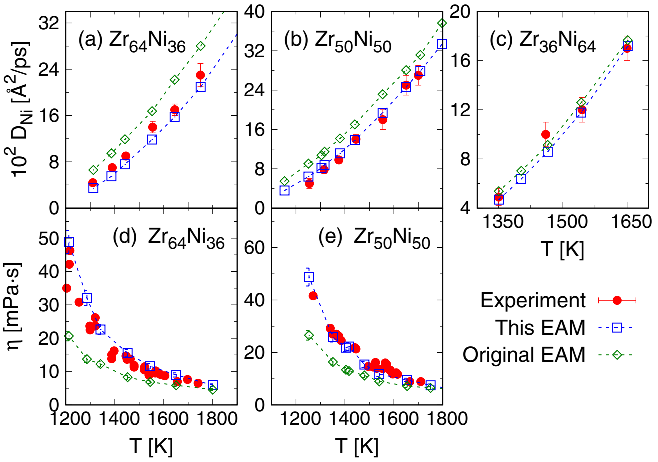

FIG. 3. (a)–(c) Temperature-dependent diffusion coefficient D_{Ni}; (d)–(e) viscosity η in Zr-Ni liquids. Red filled circles are experimental data (diffusion coefficients from Ref. [64], viscosity from Ref. [24]), hollow blue squares are results from MD simulations using our EAM potential. Green diamonds are results obtained with the original EAM potential [38].

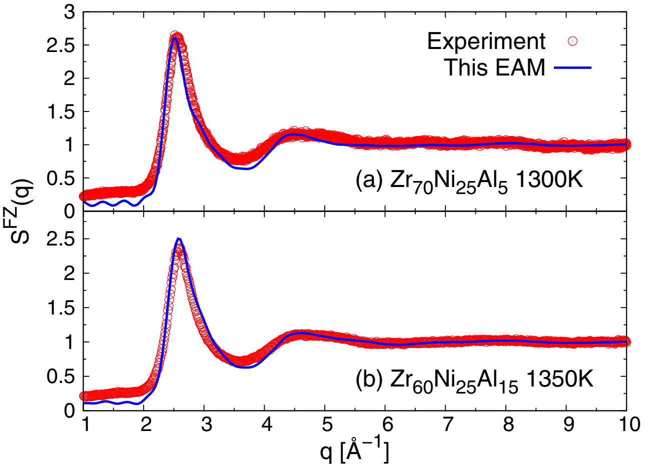

FIG. 4. Total static structure factors for $\mathrm{Zr_{70}Ni_{25}Al_5}$ (a) and $\mathrm{Zr_{60}Ni_{25}Al_{15}}$ (b) liquids at 1300 K. The red circles are experimental results measured by neutron diffraction, and the blue lines are simulation results using our EAM potential.

temperature-dependent D_{Ni} is exhibited in Figs. 3(a)–3(c) for $\mathrm{Zr_{36}Ni_{64}}$, $\mathrm{Zr_{50}Ni_{50}}$, and $\mathrm{Zr_{64}Ni_{36}}$ respectively. For the temperature and composition range investigated, we find that the simulation results coincide well with those of quasielastic neutron scattering measurement. The original EAM potential predicts a faster diffusion process than that found in experiments, especially for Zr-rich compositions. This is rectified by increasing the strength of the interatomic potential in our scaling procedure (i.e., the scaling parameter for Zr-Ni mixture is larger than unity as seen in Table I). The situation for the viscosity is quite similar, as shown in Figs. 3(d) and 3(e): Before modification, the EAM model predicts a lower viscosity than experimentally observed. Thus, the scaling procedure utilized here improves the performance of the potential in reproducing the dynamic behavior without sacrificing the accuracy of the static structure description (cf. Fig. 1).

B. Ternary mixtures

Having fixed the adjustable parameters in the procedure of the potential development, we turn to validating it for ternary Zr-Ni-Al alloys. Total static structure factors measured by neutron diffraction experiments for $\mathrm{Zr_{70}Ni_{25}Al_5}$ and $\mathrm{Zr_{60}Ni_{25}Al_{15}}$ alloys are compared with the MD results in Fig. 4. To this end, we calculated the total static structure factor $S(q)$ from MD simulation according to Eq. (4), using the neutron-scattering lengths $b_{\mathrm{Zr}} = 7.16\,\mathrm{fm}$, $b_{\mathrm{Ni}} = 10.3\,\mathrm{fm}$, and $b_{\mathrm{Al}} = 3.449\,\mathrm{fm}$ [65]. A weak composition dependence of $S(q)$ is found for these two melts. The first peak positions, peak amplitudes as well as the peak widths are well reproduced by the MD simulation. A more elaborate verification of the interatomic potential would require to compare the partial $S_{\alpha\beta}(q)$ with those measured in experiment, as in the case of binary mixture. Unfortunately, for ternary alloys six different partial structure factors must be determined, which is prohibitively difficult such that no experimentally determined partial structure factors are available for these alloys.

Figure 5 shows the Al-concentration-dependent mass density for various $\mathrm{Zr_{75-\mathit{x}}Ni_{25}Al_{\mathit{x}}}$ melts as obtained from our simulation, compared with accurate experimental data. Both the experimental data and the MD results are in reasonable agreement with each other. However, the MD simulation systematically overestimates the density at Al concentrations $x \gtrsim 0.1$. We have not found it possible to improve the EAM potential in this regard without sacrificing the accuracy in describing the structural and dynamical experimental data discussed so far, using only a set of scaling parameters applied to the functional forms of the original EAM potentials.

A comparison of the mass-transport coefficients obtained from the MD simulation with those from experiments on Zr-Ni-Al liquids is made in Fig. 6. The MD results of D_{Ni} coincide reasonably well with the experimental one, indicating a good description of the average environment for Ni atoms in dynamics. The simulated viscosity η is higher than that determined by experiments, and this tendency becomes more and more obvious at low temperatures. Thus, the shear relaxation

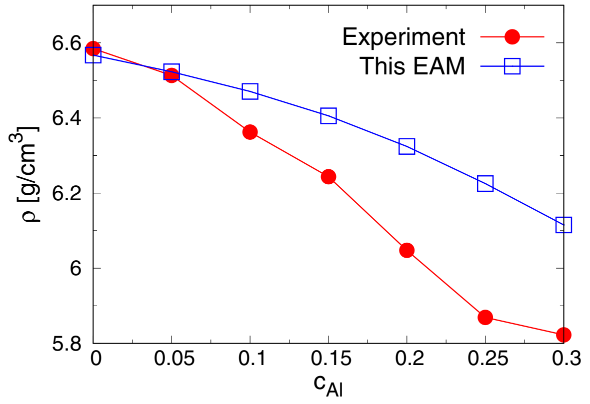

FIG. 5. Mass density $\rho_m(T)$ as a function of Al concentration $x = c_{\mathrm{Al}}$ in $\mathrm{Zr_{75-\mathit{x}}Ni_{25}Al_{\mathit{x}}}$ melts at fixed temperature $T = 1300\,\mathrm{K}$. Filled symbols are experimental measurements, open symbols the result of our MD simulations.

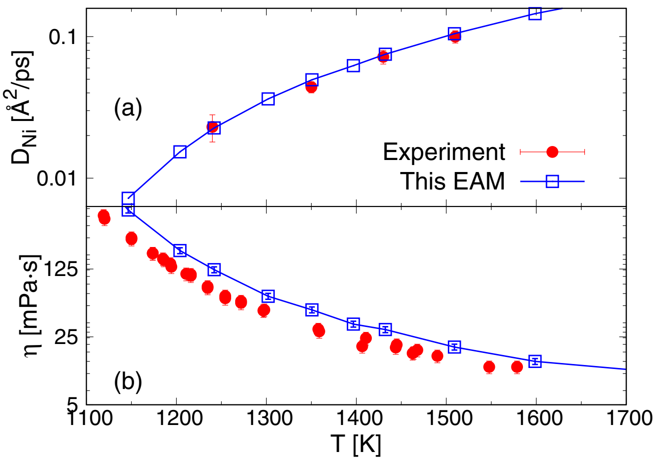

FIG. 6. (a) Temperature-dependent diffusion coefficient D_{Ni} for $\mathrm{Zr}_{60}\mathrm{Ni}_{25}\mathrm{Al}_{15}$. Red circles are experimental data from Ref. [64], blue squares are simulation results employing our EAM potential. (b) Corresponding viscosity η, experimental data from Ref. [17].

in the MD model is slower than in the experimental system. This is possibly due to an overestimation of the chemical effect caused by the Al atoms in our EAM potential (see the discussion in Sec. IV). Nevertheless, the dynamical properties described by our EAM model are qualitatively consistent with those in the real alloys, especially for the single-particle dynamics. Also, the generic trends upon changing composition are well reproduced.

IV. SIMULATION RESULTS

A. Structure

Having verified that the EAM potential is adequate to capture at least semiquantitatively the static and dynamic properties of Zr-Ni-Al melts, we proceed to a discussion of the microscopic structural changes and in particular the chemical-ordering effects introduced by the substitution of Zr through Al in $\mathrm{Zr}_{75\text{-}x}\mathrm{Ni}_{25}\mathrm{Al}_x$ ($x = 0, 5, 15, 20, 25, 30$) melts.

The partial pair correlation functions, $g_{\alpha\beta}(r)$, give the statistical information on the microstructure in terms of the reduced number density relative to the average one for finding an atom of species β at distance r from an atom of species α. There are six different pairs in the ternary mixture: Zr-Zr, Zr-Ni, Ni-Ni, Zr-Al, Ni-Al, and Al-Al. Figure 7 shows the simulation results for all these pairs at $T = 1300$ K and at different compositions. All these pair correlation functions show first peaks at distances of 2.5–3.2 Å, which correspond to the mean nearest-neighbor distances for the respective pairs of atomic species. Beyond this distance, the second peaks are seen to split into two subpeaks. The split of second peaks is attributed to the different connecting models for two nearest polyhedra in dense liquids [66], and sometimes indicative of the formation of some peculiar short-range order [13].

Zr and Ni are the majority components in $\mathrm{Zr}_{75-x}\mathrm{Ni}_{25}\mathrm{Al}_x$ ($x < 25$) melts. The first peak positions of their pairs, i.e., Zr-Zr, Zr-Ni, and Ni-Ni, shown in Figs. 7(a)–7(c), almost do not change with $x = c_{\mathrm{Al}}$. With increasing Al content we clearly see a shortening of the distances associated with the third and/or second peaks, which is indicated by the dotted and dash-dotted lines in the figure. For the pairs with Al, i.e., Al-Zr, Al-Ni, and Al-Al, most of the peak positions do not exhibit a remarkable shift (although one exception is the third-peak position for Al-Zr pairs), as shown in Figs. 7(d)–7(f). In the Al-Al partial pair correlation function, the peak at around $r \approx 5$ Å evolves as a double-peak upon increasing c_{Al} from zero, and at a further increase of the Al concentration, a prepeak emerges around $r \approx 2.5$ Å in addition [at values $c_{\mathrm{Al}} \gtrsim 20\%$, cf. Fig. 7(f)]. The prepeak in the Al-Al pair is designated as the first peak as it is responsible for the nearest-neighbor shell. The first-peak amplitude for the Al-Zr pair is much higher than all other peaks in the RDFs, indicating a strong preference for formation of these pairs. Therefore, the Al atoms show mutual self-avoidance but prefer to be the nearest neighbors of the Zr atoms.

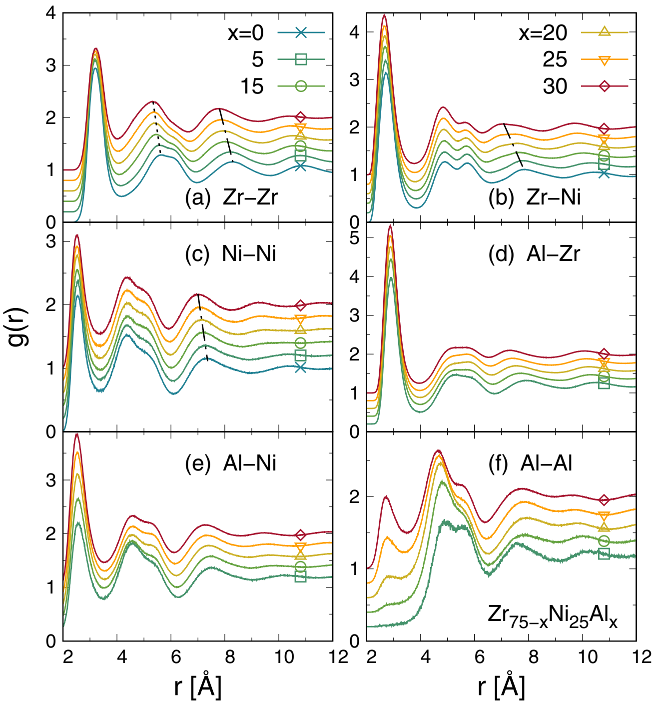

FIG. 7. Partial pair distribution functions for different atomic pairs in Zr-Ni-Al liquids obtained from MD simulation at $T = 1300$ K. Curves for different $x = c_{\mathrm{Al}}$ are offset along the vertical axis for clarity. Dotted (dash-dotted) lines are guides to the eye for the second-peak (third-peak) positions.

As a further cross-check we compare the first peak positions of the Al-related pair distribution function with *ab initio* calculations of Ref. [67] in Table II. The latter simulations have been performed for $\mathrm{Zr}_{53}\mathrm{Cu}_{18.5}\mathrm{Ni}_{12}\mathrm{Al}_{16.3}$ and are taken as a basis for comparison under the assumption that Ni and Cu have similar atomic properties and that the Zr-concentration dependence has minor influence on the peak positions [67]. Also the first peak in $g(r)$ for the Al-Al pair has been obtained in our simulation for $c_{\mathrm{Al}} = 0.30$, to increase the strength of the first Al-Al peak whose position has weak Al-concentration dependence [see in Fig. 7(f)]. As seen from Table II, the peak-position values obtained from our EAM potential are consistent with the results calculated from the *ab initio* simu-

TABLE II. Comparison on the first peak positions of Al-related pair distribution functions with *ab initio* calculation for $Zr_{60}Ni_{25}Al_{15}$ at 1300 K [67].

First peak in $g(r)$	This EAM (Å)	*ab initio*[a] (Å)
Al-Zr	2.90	2.95
Al-Ni	2.57	2.50
Al-Al	2.73[b]	2.71

[a] Data for $Zr_{53}Cu_{18.5}Ni_{12}Al_{16.3}$.

[b] Obtained for $Zr_{45}Ni_{25}Al_{30}$.

lations, to within about 3% deviation. This indicates that the major static structural feature of the Zr-Ni-Al alloys has been captured by our EAM potential, especially for the Al-related interactions.

Note that the amplitude of the first peak in the Al-Al distribution function is much weaker in our EAM simulation than found from the *ab initio* simulation. The first peak is clearly distinguishable when $c_{\rm Al} \approx 12.3\,\%$ in the *ab initio* calculation (see Fig. 1 in Ref. [67]), while it is almost absent at this concentration in our MD simulation. The weakening of the first peaks, nevertheless, can also be observed in the *ab initio* calculation where its amplitude is weaker than the one of the second peak. Thus, we assert that the chemical effect induced by the Al atoms has been captured in the developed EAM potential but overestimated to some extent.

The packing around a certain type of atomic species can be quantified by the partial coordination number, $Z_{\alpha\beta}$, which is the average neighbor number of neighbors of type β around atoms of type α. It can be calculated from the partial pair distribution functions by

$$Z_{\alpha\beta} = 4\pi\rho c_\beta \int_0^{r_c} r^2 g_{\alpha\beta}(r)\,dr, \tag{5}$$

where ρ is the average number density, c_β is the concentration of atomic type β, and r_c is the first minimum distance in the partial radial distribution function. The total coordination number for atoms of type α is $Z_\alpha = \sum_\beta Z_{\alpha\beta}$. In the case of random substitution, the neighbors around certain atom are randomly chosen according to their concentrations. This gives for the ratio of coordination numbers: $Z_{\alpha\beta}/Z_\alpha = c_\beta$, independent of the type of the central atom.

We calculated the change in coordination around Al atoms when Zr atoms are substituted by Al atoms in Zr-Ni-Al alloys. The MD results are exhibited in Fig. 8, together with the predicted values for the case of random substitution (the black dotted, dashed, and dash-dotted lines), with the specific values listed in Table III. Clear deviations are observed for all of the three atomic coordinations around the central Al atoms. With the increase of $c_{\rm Al}$, the ratios of the coordination numbers deviate more and more severely from the random substitution case, for both Zr and Al atoms. The ratio is higher than for the random substitution scenario for Zr coordinations, but lower for Al coordinations, implying that Al atoms are avoided as nearest neighbors of Al atoms but are favored as nearest neighbors of Zr atoms. For Ni atoms (that are kept at constant molar fraction), the ratio is almost unchanged ($\approx$0.3) with the value still higher than expected for random substitution (=0.25). These biases for the atomic species-dependent coordination number indicate a strong chemical interaction between Al and the other atomic species.

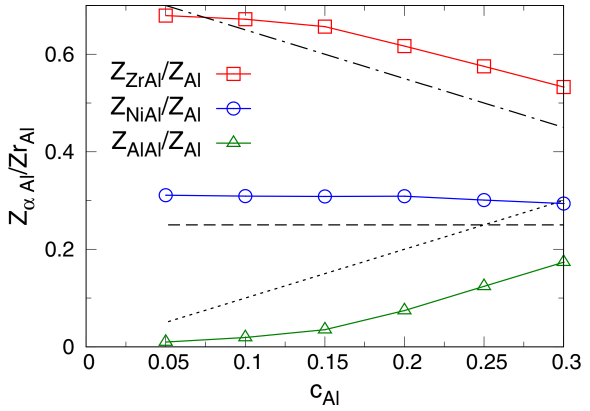

FIG. 8. Ratios of coordination numbers around a central Al atom in $Zr_{75-x}Ni_{25}Al_x$ liquids as a function of Al concentration $x = c_{\rm Al}$. The dotted and dash-dotted lines are values expected from random substitution.

Besides the short-range order in terms of the preferred coordinated atoms, the chemical interaction also affects the packing structure further beyond. For this purpose, peak positions from first to third shells for the matrix components are extracted from Fig. 7, shown in Fig. 9. First, for all these pairs, the first-neighbor distances are almost independent on $c_{\rm Al}$. Thus the addition of Al up to $c_{\rm Al} = 0.30$ does not affect the atomic interaction radii of the other species. A systematic trend can be identified in the second and third-neighbor distances, bearing in mind that there is a nontrivial second-nearest-neighbor shell structure indicated by a splitting of the second peaks in $g_{\alpha\beta}(r)$. As shown in Fig. 9, in particular the third-nearest Zr and Ni neighbors of Zr and Ni atoms move closer by addition of Al, i.e., admixture of Al serves to locally densify the structure of Zr-Ni.

For an analysis of the structural changes induced by the addition of Al, we compare the mean distance of heteroatomic Zr-Al and Ni-Al nearest neighbors with the mean distances estimates from the sizes r_α of the corresponding atomic species. As a simple estimate of these atomic sizes, we take the nearest-neighbor distances obtained from the first-peak positions in $g_{\alpha\beta}(r)$. Then the reduced ratios of the heterogeneous radii are $2r_{\alpha\beta}/(r_\alpha + r_\beta) - 1$. This gives values of -2.2% to -3.4% and -2.5% to -5.5% found for Zr-Al and

TABLE III. Values of the first-peak positions and the calculated partial coordination number for the pairs with Al atoms.

	$r^{(1)}_{\alpha\beta}$ (Å)			$Z_{\alpha\beta}$		
$c_{\rm Al}$	Al-Zr	Al-Ni	Al-Al	Al-Zr	Al-Ni	Al-Al
0.05	2.91	2.55	–	9.77	2.68	0.04
0.10	2.90	2.57	–	9.64	2.75	0.11
0.15	2.90	2.57	–	9.32	2.83	0.25
0.20	2.88	2.52	2.81	8.91	3.01	0.65
0.25	2.87	2.52	2.75	8.26	3.05	1.26
0.30	2.90	2.57	2.73	7.61	3.12	2.02

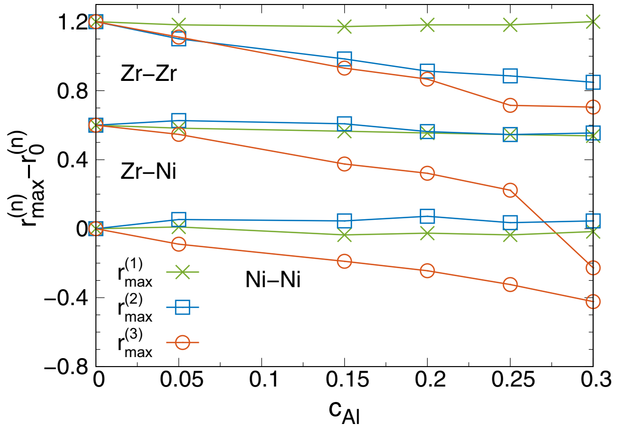

FIG. 9. Concentration-dependent peak positions at 1300 K for Zr-Zr, Zr-Ni, and Ni-Ni partial RDFs. The cross symbols are for the first-peak positions, $r_{\rm max}^{(1)}$, squares are for the second-peak positions, $r_{\rm max}^{(2)}$, and circles are for the third-peak positions, $r_{\rm max}^{(3)}$. $r_0^{(n)}$ is the nth peak position at $c_{\rm Al} = 0$. For clarity, the results for Zr-Ni and Zr-Zr pairs are shifted upward by 0.6 and 1.2, respectively.

Ni-Al pairs respectively, indicating a shrinkage of the hetero-atomic bonds. A similar shortening of bonds was observed by elastic neutron scattering experiments on binary alloys melts of Zr-Ni, Nb-Ni, and Hf-Ni [11]. The reduced interatomic distance implies an affinity between different atomic species, although it is not necessary to densify the local structure in the second shell as like for the Zr-Ni and Ni-Ni pairs.

B. Transport coefficients

Having elucidated the static structural features of the melts, we turn to dynamical properties of mass transport. We focus on the transport coefficients that are usually assessed in experiment to quantify the liquid dynamics, *viz.*, the self-diffusion coefficients that describe the mobility of single particles, and the shear viscosity that serves as a proxy for the structural relaxation of the system.

The composition-dependent self-diffusion coefficients are shown in Fig. 10. The value of $D_{\rm Zr}$ is found to be smaller than that of $D_{\rm Ni}$ which is expected from entropic arguments as Zr atoms are heavier and bigger than the Ni atoms. But although Al atoms are smaller in atomic radius than Zr, $D_{\rm Al}$ is found to be lower than the diffusion coefficients of the other species, and close to $D_{\rm Zr}$. This indicates a breakdown of the hard-sphere analogy, where smaller species should show faster diffusion. It can be attributed to strong interactions of Al with the other species, which counterbalances the entropic enhancement of mobility (as suggested by the hard-sphere analogy) and leads to overall lower mobility due to chemical effects. A reduced mobility for Al atoms has also been found in Zr-Cu-Al alloys, where $D_{\rm Cu} > D_{\rm Al} > D_{\rm Zr}$ was reported [20]. All self-diffusion coefficients decrease monotonically with $c_{\rm Al}$, approaching to almost the same value at $c_{\rm Al} = 0.3$ especially for Al and Zr atoms. Strong coupling between unlike atoms can make the diffusivities of different species alike to each other. Recall that structurally, Zr and Al pairs are preferred, so that the slow diffusivity of Al atoms can be rationalized as a result of the strong coupling of Zr-Al pairs. A related phenomenon involving strong chemical preference to link the related self-diffusion coefficients has also been found in Zr-Ni and Au-Al binary mixtures [9,13].

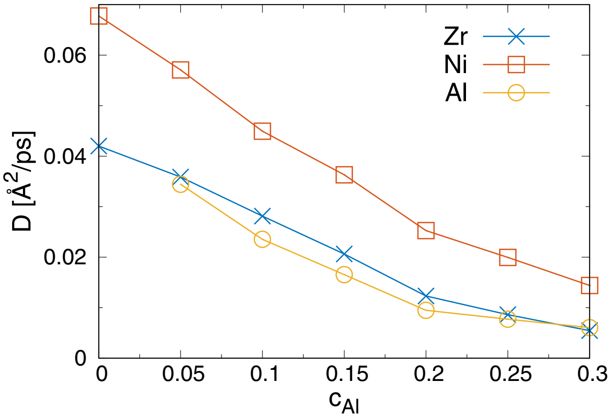

FIG. 10. Al-concentration-dependent self-diffusion coefficients D_α in Zr-Ni-Al melts as obtained from our MD simulations.

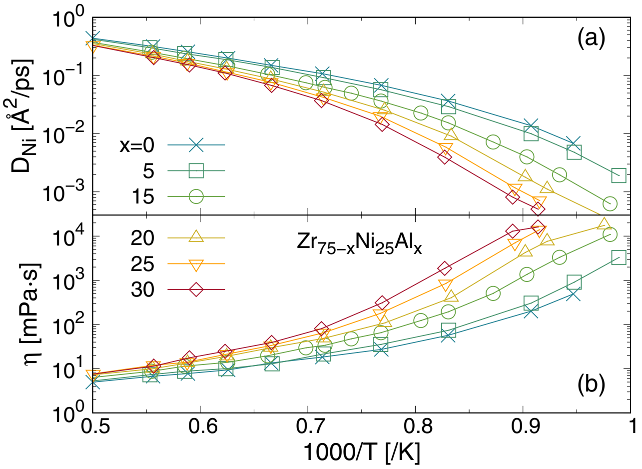

FIG. 11. Temperature-dependent D (a) and η (b) calculated from the MD simulation.

The temperature-dependent D and η are shown in Fig. 11. At high temperatures, these transport coefficients can be described by the Arrhenius law, i.e., D or $1/\eta \sim \exp[E_A/k_BT]$, where E_A is the temperature-independent activation energy. We observe that the Arrhenius behavior gradually breaks down as the temperature is decreased; cf. Figs. 11(a) and 11(b) both for D and η. The breakdown is usually attributed to the emergence of atomic collectivity in space [68–71], or equivalently, the transition from simple liquid to cooperative liquid [25]. A clear shift of this transition point to higher temperature with Al concentration can be observed both for D and η. This indicates that the motion of atoms becomes cooperative at higher temperatures with increasing $c_{\rm Al}$. For the low-temperature super-Arrhenius behavior, we see that the activation energy (which is temperature-dependent, calculated as the slope value in the semilogarithm plot) becomes higher with $c_{\rm Al}$ as seen in Fig. 11. This implies a larger activation volume or cooperative region. Therefore, the chemical interaction in this ternary system increases not only the crossover

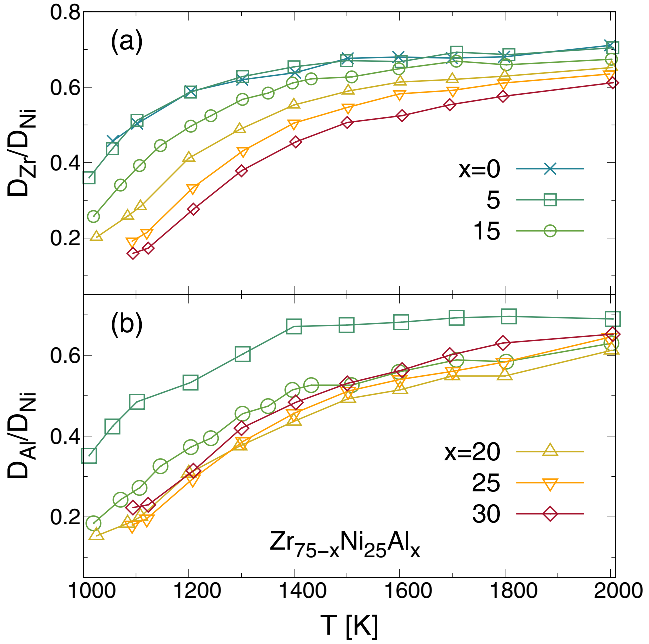

FIG. 12. Temperature-dependent diffusion ratios with respect to the Ni atoms for Zr (a), and Al (b).

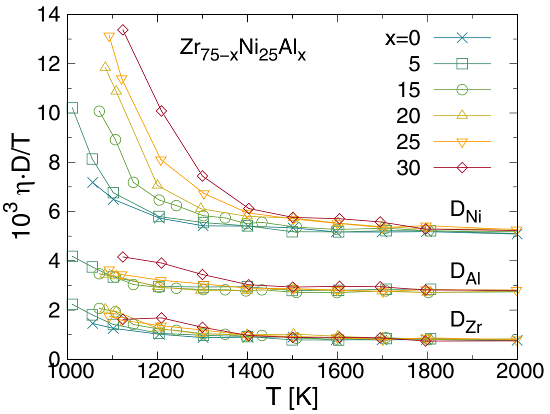

FIG. 13. SE relation using three different self-diffusion coefficients. For clarity, the curves have been shifted along the *y* axis by unit 2 and 4 for the case of $D_{\rm Al}$ and $D_{\rm Ni}$.

temperature where the cooperative movement emerges, but also the spatial correlation range. A similar high-temperature shift of this crossover point has also been reported experimentally in Zr-Ni/Co-Al [17] and Hf-Zr-Ni [72] melts.

Another method to characterize the collectivity of atomic motion is the mass effect (or isotope effect) [73]. At high temperature or in the low-density limit, binary collisions dominate the dynamics of the system, and the motion of the atoms becomes uncorrelated. Considering that different atomic species are in the same thermal bath, i.e., $\langle m_\alpha \mathbf{v}_\alpha^2\rangle = 3k_BT$, which gives $\langle|\mathbf{v}_\alpha|\rangle \propto \sqrt{T/m_\alpha}$. Then, at the same temperature, the ratio of the diffusivities is $D_\alpha/D_\beta = \sqrt{m_\beta/m_\alpha} =$ const. In this ternary system, the diffusivity ratios expected under these assumptions are $D_{\rm Zr}/D_{\rm Ni} = 0.8$ and $D_{\rm Al}/D_{\rm Ni} = 1.5$. The temperature-dependent diffusivity ratios calculated by MD simulation are shown in Fig. 12. For a $\rm Zr_{75}Ni_{25}$ melt at $T = 2000$ K, $D_{\rm Zr}/D_{\rm Ni} \approx 0.7$, which is close to the value predicted by the isotopic effect. But for $D_{\rm Al}$ and $D_{\rm Ni}$, the ratio is about 0.7, i.e., far below the prediction. Thus, Zr atoms are more or less uncorrelated with Ni atoms, but strongly correlated with Al even at high temperatures.

Despite the deviation from the mass effect, the temperature-independent constant D_α/D_β indicates a situation of an unchanged cooperative environment for these two atomic species on average. Upon cooling, the constants become temperature-dependent, implying that the cooperative behavior changes. The onset of this transition shifts to higher temperatures with increasing $c_{\rm Al}$. For instance, $D_{\rm Zr}/D_{\rm Ni}$ becomes temperature-dependent at around 1400 K for $\rm Zr_{75}Ni_{25}$, but at around 1800 K or even higher temperature for $\rm Zr_{50}Ni_{25}Al_{25}$ melts [see Fig. 12(a)]. Thus, atoms become collective earlier in Al-rich melts upon cooling. Another interesting question is whether the ratios, $D_{\rm Zr}/D_{\rm Ni}$ and $D_{\rm Al}/D_{\rm Ni}$, both become temperature-dependent at the same temperature or not. For the Al-poor composition, $\rm Zr_{70}Ni_{25}Al_5$, both these ratios become temperature-dependent at the same temperature, i.e., 1400 K. But for the other melts, due to the data inaccuracy and high critical temperature for this dependence (about 1800–2000 K or even higher), it is hard to assert.

The diffusion coefficient and shear viscosity can be related by SE relation, i.e., $D_\alpha\eta = k_BT/(cd_\alpha)$, where d_α is the effective diameter of the diffusing species and c is a constant ($= 2\pi$ for slip boundary condition and 3π for stick boundary condition). Although the SE relation is originally derived for a macroscopic particle diffusing in a solvent of particles of much smaller size, it holds surprisingly well in atomic or molecular liquids. The SE relation usually breaks down at low temperatures (typically below the mode-coupling transition T_c), due to the growth of atomic collective movement, e.g., the heterogeneous dynamic fluctuation in space and time [68,74,75], or equivalently the separation of fast and slow particles [76,77]. Figure 13 shows the SE ratio for the three self-diffusion coefficients in this ternary mixtures. First, the violation of SE relation is more obvious in the case of $D_{\rm Ni}$ than the other two. Weak violation is seen at T < 1800 K for $D_{\rm Ni}$, and strong at T < 1200–1400 K. In the case of $D_{\rm Zr}$ and $D_{\rm Al}$, there is only weak violation observed at T < 1400 K. Specifically, we observe a six to eight times increment for $D\eta/T$ at low temperatures for $D_{\rm Ni}$, but only an increment by less than a factor two for $D_{\rm Zr}$ and $D_{\rm Al}$. Thus, the violation of SE is more significant if utilizing fast particle's diffusivity (Ni atoms) than using slow ones (Zr or Al atoms). This is due to the fact that shear relaxation is mostly affected by densely packed particles, which are also slow in single-particle dynamics. In a subsystem of slow particles, the SE relation can be even recovered if the corresponding diffusion coefficient is used [77].

For the breakdown of the SE relation, the onset point systematically shifts to higher temperatures with increasing $c_{\rm Al}$, and the intensity also grows (see Fig. 13 for $D_{\rm Ni}$). This is expected because the chemical effect is strengthened with Al addition, similar to the situation of a super-Arrhenius transition for the transport coefficients shown in Fig. 11. A simple parameter to predict the breakdown of the SE relation

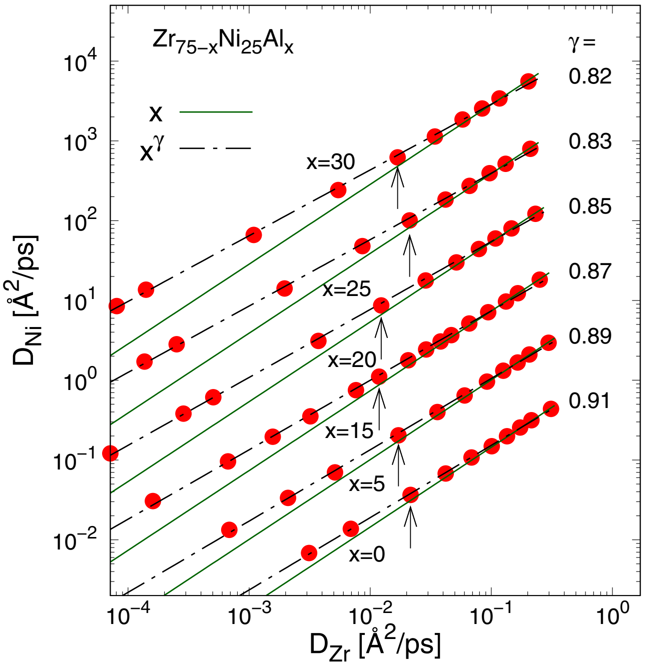

FIG. 14. Power-law dependence of the diffusion coefficients in Zr-Ni-Al melts with different Al concentration. The curves are shifted along the y axis for clarity. Both solid lines and dash-dotted lines are power-law fitting, differing in the fitting method (see text for details). The arrows indicate the onset points of strong SE violation.

is D_α/D_β, with the onset point for its temperature dependence predicting the point for the breakdown of the SE relation. This has been verified in binary metallic mixtures [18,19]. The ratios D_{Zr}/D_{Ni} and D_{Zr}/D_{Ni} exhibit drastic drop upon cooling at about 1200 K for Al-poor compositions (e.g., $Zr_{75}Ni_{25}$ and $Zr_{70}Ni_{25}Al_5$), and at about 1400 K for $Zr_{50}Ni_{25}Al_{25}$ melts [see Fig. 12 (a)], roughly coinciding with the onset temperatures of strong SE relation violation for D_{Ni} (see Fig. 13). But for the SE violation for slow particle's diffusivity (D_{Zr} and D_{Al}), this consistence is rather ambiguous.

The crossover from a ratio of self-diffusion coefficients that is temperature-independent to one that depends on temperature poses a puzzle for theories of the glass transition. For example, the mode-coupling theory (MCT) predicts that asymptotically close to T_c, all self-diffusion coefficients should exhibit the same temperature dependence, i.e., their ratio should approach a constant value. But it is well known that below T_c, the MCT picture breaks down, and diffusion of the individual atomic species decouples [78]. Recently, it was proposed that for a large variety of glass formers, power-law relationships might hold between the diffusion coefficients, $D_{\mathrm{fast}} \propto D_{\mathrm{slow}}^{\gamma}$, which would be consistent with an Adam-Gibbs picture of relaxation [79]. The exponent γ was found to be generally less than unity, but nonuniversal among a number of computer-simulation models that have been investigated.

Also in our computational model, the same observation applies, as shown by a double-logarithmic plot of D_{Ni} versus D_{Zr} (Fig. 14); similar results would be obtained for D_{Al}. As expected from the isotopic effect, at high temperatures, the diffusion coefficients become proportional to each other to within the numerical uncertainty, i.e., $\gamma = 1$ is approached. Below an onset temperature that corresponds to a roughly constant value of D_{Zr}, deviations that were already manifest in Fig. 13 can be identified; in this regime of low diffusivity, a power law with an exponent $\gamma < 1$ describes the data reasonably well. The data could be fitted with almost equal quality by this single power law over the whole range shown in Fig. 14, similar to what has been discussed in Ref. [79]. This points to the fact that such fits represent effective power laws that span a crossover region. It is still unclear that how this effective power law could describe both the dynamics in normal liquids and the slow one at low temperatures. A rigorous testing this prediction would require a much broader data range, as for example recently discussed in an extension of MCT [80]. Nevertheless, we find that the exponent of the effective power-law fitting shows a monotonic tendency with the Al concentration, that is close to unity at small c_{Al}, but clearly lower than unity at larger c_{Al}. A smaller value of the exponent, γ, could indicate a stronger chemical interaction in the series of alloys we investigated.

C. Acoustic excitation

The time-dependent collective motion of atoms in density fluctuation can be described by the dynamic scattering function, which is defined as

$$S(q,t) = \frac{1}{N}\sum_{i,j} e^{-i\mathbf{q}\cdot[\mathbf{r}_i(t)-\mathbf{r}_j(0)]}. \tag{6}$$

In its Fourier transformation, $S(q,\omega)$, the longitudinal collective modes of the melt dynamics manifest themselves. The spectrum as a function of wave vector q and c_{Al} is shown in Fig. 15. In order to let $S(q,t)$ decay to zero for the accessible q waves in the simulation time scale, the spectrum is calculated at relatively high temperature, 1600 K. There are two clear peaks: one is centered at $\omega = 0$ presenting the diffusive modes due to thermal diffusivity and interdiffusivity, and the other one is centered at finite frequency presenting the longitudinal acoustic mode. With increasing wave vector, the diffusive peak becomes broader and the acoustic peak shifts to higher frequencies. This is typical behavior of the hydrodynamic modes. In multicomponent liquids, the hydrodynamic regime for the macroscopic adiabatic sound wave is often so narrow that it could be below the resolution limit set by the lowest accessible **q** vector investigated in our simulations. The collective excitation observed is because of the disparate atomic mass and often referred as "fast sound" mode [81]. A notable phenomenon is that the fast sound peak shifts to higher frequencies with the addition of Al, if the wave vector is kept constant. This indicates that the fast sound waves propagate faster in the melts with higher Al concentrations.

At $\omega \approx 50$ ps^{-1}, an subpeak emerges at $q = 1.2$ Å^{-1} for the compositions with Al addition. The positions of this subpeak do not change with the q-wave vector. This is reminiscent of the optic phonons in crystals, whose vibration frequency is typically independent of the wave vector. Optic phonons in crystals are well defined and correspond to the motion of nearest neighbors of different atomic species that vibrate in opposite directions. This motion is usually induced by differently signed ions like in crystalline salt or by mass

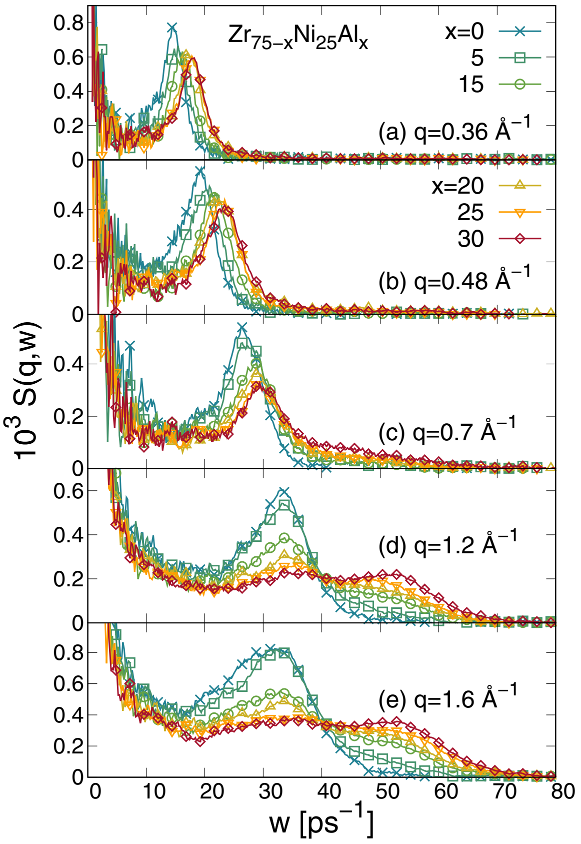

FIG. 15. Dynamic scattering functions for Zr-Ni-Al liquids at $T = 1600$ K, at different wave vectors ranging from 0.36 to 1.6 Å^{-1} (a–e).

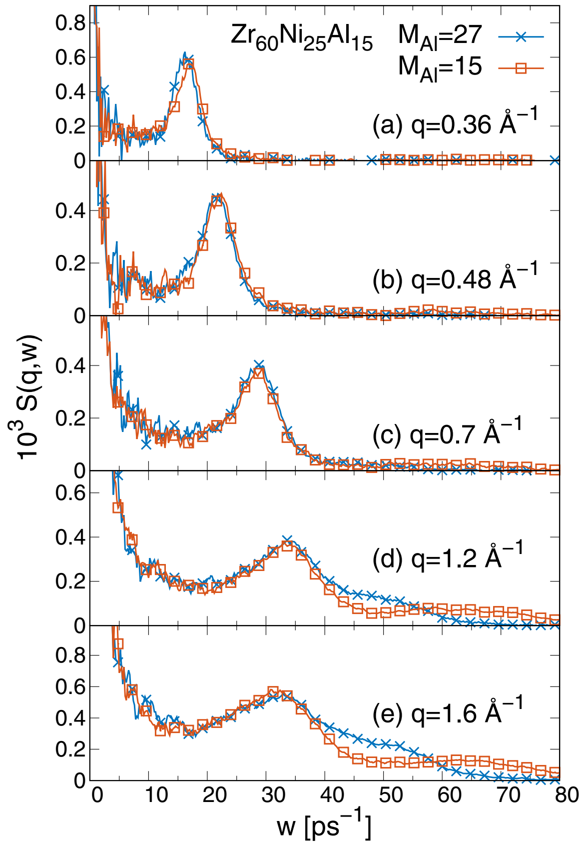

FIG. 16. Dynamic scattering functions for $Zr_{60}Ni_{25}Al_{15}$ liquids at $T = 1600$ K, for different wave vectors ranging from 0.36 to 1.6 Å^{-1} (a–e). The blue crosses are the results for Al atoms with normal mass (=27 g/cm^3), while the red squares are the reduced Al mass case (=15 g/cm^3).

differences of the different species. In the Zr-Ni-Al ternary mixtures, the Al atoms are considerably lighter than the Zr or Ni atoms. Lighter Al atoms could induce opticlike motion in the matrix formed by the heavier Zr and Ni atoms. To verify this assumption, we reduce the molar mass of Al atoms from 27 g/cm^3 to 15 g/cm^3, with all the other force-field parameters unchanged in the simulation model. The resulting spectrum for the reduced Al mass is plotted in Fig. 16. For the hydrodynamic modes, there is no observable change. But the subpeak positions, ω_p, shift from 50 to 65 ps^{-1}. In the case of crystalline structure, the excitation frequency of optic modes is dependent on $1/\sqrt{m_h}$ and $1/\sqrt{m_l}$, where m_h and m_l are the mass of heavy and light atoms, respectively, in binary systems [82]. In the MD simulation, the excitation frequency roughly shifts by $65/50 = 1.3$, coinciding with the shift predicted for crystals when changing the Al mass (where $\sqrt{27}/\sqrt{15} = 1.34$). Because the optic modes are high-frequency excitations in crystals, the opticlike modes are usually not expected to occur in liquids. This result shows that a similar opticlike excitation exists in multicomponent melts like in the crystalline state. Such opticlike excitations have also been reported for binary liquids with the theoretical approach of generalized collective modes [83,84].

A typical dispersion relation for the fast acoustic wave is shown in Fig. 17(b). It has been determined by picking up the peak positions of $S(q, \omega)$. At low wave vectors, a linear relationship is found, giving the longitudinal sound velocity. Separating $S(q, \omega)$ into contributions from the different pairs, $S^{\alpha\beta}(q, \omega)$, highlights that the subpeaks are resulting completely from the Al-Al pairs [as seen in Fig. 17(a)]. The branch obtained from $S^{\mathrm{AlAl}}(q, \omega)$ shows almost a constant excitation frequency at about 50 ps^{-1}, i.e., an opticlike mode, for large wave vectors. At small wave vectors, this opticlike mode is unobservable, and what it picks up is the acoustic wave coinciding with that at total $S(q, \omega)$. A more sophisticated approach to unveil the optic excitation is calculating the partial longitudinal or transverse current spectral functions as done for binary [83] and ternary liquids [85].

The concentration-dependent acoustic velocity is shown in the inset picture [Fig. 17(c)]. The fast sound velocity grows with increasing Al concentration. In order to assert the density effect on the acoustic propagating velocity, we scale the velocity with the mass density, i.e., $V_s\sqrt{\rho}$ versus c_{Al}, finding similar behavior with that of no-density scaling (result is not shown here). Failure of the density scaling indicates the increment of sound velocity is due to the enhanced collectivity rather than the change of density in the compositions of Al addition.

V. CONCLUSION

To accurately predict the microstructure and dynamics of Zr-Ni-Al melts, we have developed an effective EAM

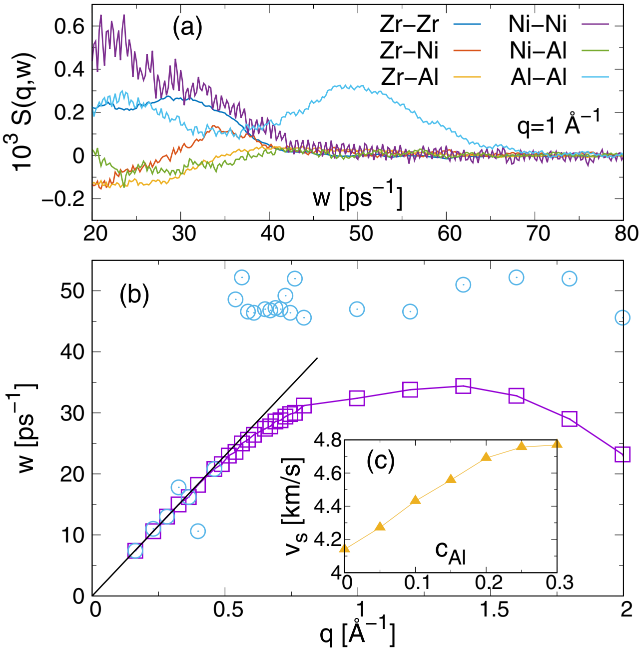

FIG. 17. Partial dynamic structure factors, $S^{\alpha\beta}(q,w)$, for different pairs in $Zr_{60}Ni_{25}Al_{15}$ liquids (a) and the dispersion relation in the same composition (b). The purple squares in panel (b) are the longitudinal model extracted from the total $S(q,\omega)$, while the cyan circles are the opticlike model extracted from the Al-Al partial dynamic scattering function $S^{\mathrm{AlAl}}(q,\omega)$. The black line is the linear fitting at small wave vectors. The inset panel (c) shows the sound velocity as a function of the Al concentration obtained from the dispersion relation at $T = 1600$ K.

potential. The potential bases on existing force fields for the binary Zr-Ni and Al-Ni systems and is gauged against new accurate data on structure and mass-transport coefficients of liquid Zr-Ni-Al melts, some of which were specifically obtained for the present project. To reduce the complexity of regauging the previously existing binary EAM potentials that were mainly gauged against crystalline states, we introduce a set of distance scaling parameters r_s (roughly corresponding to adjustments needed to describe the static structure), and a set of strength parameters λ (roughly mapping to dynamical behavior). A broad set of experimental data is utilized for the potential validation, specifically mass densities, partial static structure factors, diffusivities, and viscosities.

We emphasize that the ternary potential developed is *ad hoc* for the liquid state of Zr-Ni-Al alloys. Accurate description of the crystalline state is not guaranteed in this model. It can be seen that the energetic terms are scaled by the parameter λ. This could lead to an inaccurate estimation of the cohesive energy and lattice constants in the crystals. But the potential is substantially validated on the aspect of the static structure in liquid state including partial $S(q)$ in Ni-Al and Zr-Ni melts, total ones in Zr-Ni-Al liquids that importantly contains the information of the nearest interaction distance and the chemical short-range order (in terms of the prepeaks in the binary mixtures), as well as the transport coefficients in different temperatures and compositions. We thus believe our model to be accurate for the description of structure-dynamics relationships in the liquid state of the ternary alloy.

Based on the potential, we conducted MD simulations in a series of compositions of $Zr_{75-x}Ni_{25}Al_x$ ($x = 0-30$) melts, where the effect of chemical interaction induced by Al atoms was investigated. From the partial pair distribution functions, we find a strong coordination bias in the nearest-neighbor shell, where Al atoms exhibit strong preference to stay close to Ni and in particular Zr atoms, but a structural avoidance of Al atoms among themselves. This locally preferred structure has a much shorter atomic interaction distance than that expected from a hard-sphere model, if one assigns to the Al atoms a typical empirical atomic radius. For the medium-range structure, we found a drastic shortening of the third-shell distance on the substitution of Zr atoms by Al atoms for all the atomic pairs in the Zr-Ni matrix.

The locally preferred structure imposes significant influence on the mass transport process of the liquids. For the self-diffusivities calculated from the MD simulations, the concentration-dependent behavior shows a tendency of approaching alike with c_{Al}, especially for Al atoms and Zr atoms, indicating strong coupling between them. The mass effect, on the other hand, elucidates the correlated dynamics between different atoms: Zr atoms are to some extent uncorrelated with Ni atoms, but strongly correlated with Al even at high temperatures.

Upon cooling down, the temperature dependence of transport coefficients usually exhibit a deviation from the simple Arrhenius law. This transition is an indicator for the emergence of cooperative motion in the liquids [69,70,86]. In our simulation model, onset points of the Arrhenius-to-super-Arrhenius transition for the diffusivities and shear viscosities occur at higher temperature in the alloys of higher Al concentration, suggesting that the onset of collective motion occurs earlier.

The SE relation that relates the self-diffusivity and shear viscosity, breaks down in the vicinity of the super-Arrhenius transition. Remarkably, the SE relation is reasonably well fulfilled over the temperature range accessible in the MD simulations, when no Al is present, even for the "smallest" atom, i.e., for D_{Ni}. In the systems with small amounts of Al, a violation of the SE relation is observed for all three atomic species, but still the strongest violations are seen for Ni. In other words, Al addition causes stronger violations of the SE relation not predominantly because Al atoms are small and couple less strongly to the collective structural relaxation, but rather because they induce collective structural changes. This again points to the role of addition of small quantities of Al: they act as a structural-change agent, rather than just a fast-diffusing species.

Decoupling of these different dynamical processes has also been demonstrated in terms of the relation between fast and slow atoms' diffusivities, where an effective power-law behavior is found with the exponent decreasing on the decreasing of Al concentration. The deviation point for the effective power-law description with the isotopic prediction coincides with the onset points of the SE violation.

For the vibrational motion of atoms, we find an opticlike mode from the dynamic scattering functions in the high-temperature Zr-Ni-Al liquids. The excitation frequency of the opticlike mode is approximately proportional to $1/\sqrt{M_{\mathrm{Al}}}$ (contribution from the heavier atoms is neglected). On the other hand, the fast sound wave propagates faster at higher Al concentrations, which we ascribe to the chemical interaction introduced by Al rather than the density effect.

ACKNOWLEDGMENTS

H.L.P. acknowledges funding from the German Academic Exchange Service (DAAD) for funding through the DLR-DAAD program under Grant No. 131. We thank A. Meyer and H. R. Schober for very stimulating discussions.

[1] W. H. Wang, Prog. Mater. Sci. **52**, 540 (2007).
[2] J. D. Bernal, Nature (London) **185**, 68 (1960).
[3] P. H. Gaskell, Nature (London) **276**, 484 (1978).
[4] S. M. Chathoth, B. Damaschke, M. M. Koza, and K. Samwer, Phys. Rev. Lett. **101**, 037801 (2008).
[5] F. Yan, D. Holland-Moritz, J. Gegner, P. Heintzmann, F. Kargl, C. C. Yuan, G. G. Simeoni, and A. Meyer, EPL **107**, 46001 (2014).
[6] S. M. Chathoth, A. Meyer, M. M. Koza, and F. Juranyi, Appl. Phys. Lett. **85**, 4881 (2004).
[7] I. Kaban, P. Jóvári, V. Kokotin, O. Shuleshova, B. Beuneu, K. Saksl, N. Mattern, J. Eckert, and A. L. Greer, Acta Mater. **61**, 2509 (2013).
[8] A. Yakymovich, I. Shtablavyi, and S. Mudry, J. Alloys Compd. **610**, 438 (2014).
[9] T. Voigtmann, A. Meyer, D. Holland-Moritz, S. Stüber, T. Hansen, and T. Unruh, EPL **82**, 66001 (2008).
[10] B. Nowak, D. Holland-Moritz, F. Yang, T. Voigtmann, T. Kordel, T. C. Hansen, and A. Meyer, Phys. Rev. Materials **1**, 025603 (2017).
[11] B. Nowak, D. Holland-Moritz, F. Yang, T. Voigtmann, Z. Evenson, T. C. Hansen, and A. Meyer, Phys. Rev. B **96**, 054201 (2017).
[12] J. Qin, X. Bian, S. I. Sliusarenkodag, and W. Wang, J. Phys.: Condens. Matter **10**, 1211 (1998).
[13] H. L. Peng, T. Voigtmann, G. Kolland, H. Kobatake, and J. Brillo, Phys. Rev. B **92**, 184201 (2015).
[14] M. Maret, T. Pomme, A. Pasturel, and P. Chieux, Phys. Rev. B **42**, 1598 (1990).
[15] S. K. Das, J. Horbach, M. M. Koza, S. M. Chatoth, and A. Meyer, Appl. Phys. Lett. **86**, 011918 (2005).
[16] Y. Q. Cheng, E. Ma, and H. W. Sheng, Phys. Rev. Lett. **102**, 245501 (2009).
[17] C. C. Yuan, F. Yang, F. Kargl, D. Holland-Moritz, G. G. Simeoni, and A. Meyer, Phys. Rev. B **91**, 214203 (2015).
[18] X. J. Han and H. R. Schober, Phys. Rev. B **83**, 224201 (2011).
[19] X. J. Han, J. G. Li, and H. R. Schober, J. Chem. Phys. **144**, 124505 (2016).
[20] A. Jaiswal, T. Egami, and Y. Zhang, Phys. Rev. B **91**, 134204 (2015).
[21] J. Brillo, S. M. Chathoth, M. M. Koza, and A. Meyer, Appl. Phys. Lett. **93**, 121905 (2008).
[22] A. Jaiswal, S. O'Keeffe, R. Mills, A. Podlesynak, G. Ehlers, W. Dmowski, K. Lokshin, J. Stevick, T. Egami, and Y. Zhang, J. Phys. Chem. B **120**, 1142 (2016).
[23] Z. Evenson, F. Yang, G. G. Simeoni, and A. Meyer, Appl. Phys. Lett. **108**, 121902 (2016).
[24] J. Brillo, A. I. Pommrich, and A. Meyer, Phys. Rev. Lett. **107**, 165902 (2011).
[25] J. P. Hansen and I. R. MacDonald, *Theory of Simple Liquids*, 3rd ed. (Academic Press, Oxford, 2005).
[26] S. K. Das, J. Horbach, and T. Voigtmann, Phys. Rev. B **78**, 064208 (2008).
[27] N. Jakse, O. Lebacq, and A. Pasturel, Phys. Rev. Lett. **93**, 207801 (2004).
[28] N. Jakse, O. Lebacq, and A. Pasturel, J. Chem. Phys. **123**, 104508 (2005).
[29] N. Jakse and A. Pasturel, Phys. Rev. B **94**, 224201 (2016).
[30] N. Jakse and A. Pasturel, Phys. Rev. B **95**, 144210 (2017).
[31] Y. C. Hu, F. X. Li, M. Z. Li, H. Y. Bai, and W. H. Wange, Nat. Comm. **6**, 8310 (2015).
[32] C. H. Li, Y. W. Luan, X. J. Han, and J. G. Li, J. Non-Cryst. Solids **458**, 107 (2017).
[33] K. F. Kelton, J. Phys.: Condens. Matter **29**, 023002 (2017).
[34] F. Ercolessi and J. B. Adams, Europhys. Lett. **26**, 583 (1994).
[35] M. I. Mendelev and G. J. Ackland, Philos. Mag. Lett. **87**, 349 (2007).
[36] M. I. Mendelev, M. J. Kramer, C. A. Becker, and M. Asta, Philos. Mag. **88**, 1723 (2008).
[37] M. I. Mendelev, M. J. Kramer, R. T. Ott, D. J. Sordelet, D. Yagodin, and P. Popel, Philos. Mag. **89**, 967 (2009).
[38] M. I. Mendelev, M. J. Kramer, S. G. Hao, K. Ho, and C. Z. Wang, Philos. Mag. **92**, 4454 (2012).
[39] Y. Zhang, R. Ashcraft, M. I. Mendelev, C. Z. Wang, and K. F. Kelton, J. Chem. Phys. **145**, 204505 (2016).
[40] J. Horbach, S. K. Das, A. Griesche, M.-P. Macht, G. Frohberg, and A. Meyer, Phys. Rev. B **75**, 174304 (2007).
[41] G. P. P. Pun and Y. Mishin, Philos. Mag. **89**, 3245 (2009).
[42] S. Zhao, J. Li, and B. Liu, J. Phys. Soc. Jpn. **79**, 064607 (2010).
[43] A. Takeuchi, K. Yubuta, M. Ogata, and A. Inoue, J. Mater Sci. **45**, 4898 (2010).
[44] M. Guerdane and H. Teichler, Phys. Rev. B **65**, 014203 (2001).
[45] S. Stüber, D. Holland-Moritz, T. Unruh, and A. Meyer, Phys. Rev. B **81**, 024204 (2010).
[46] M. S. Daw and M. I. Baskes, Phys. Rev. B **29**, 6443 (1984).
[47] M. Finnis and J. Sinclair, Philos. Mag. A **50**, 45 (1984).
[48] R. A. Johnson, Phys. Rev. B **39**, 12554 (1989).
[49] P. Kuhn, J. Horbach, F. Kargl, A. Meyer, and T. Voigtmann, Phys. Rev. B **90**, 024309 (2014).
[50] S. Plimpton, J. Comp. Phys. **117**, 1 (1995).
[51] I. Egry, H. Giffard, and S. Schneider, Meas. Sci. Technol. **16**, 426 (2005).
[52] H. Lamb, Proc. London Math. Soc. **s1-13**, 51 (1881).
[53] P. Heintzmann, F. Yang, S. Schneider, G. Lohöfer, and A. Meyer, Appl. Phys. Lett. **108**, 241908 (2016).
[54] T. C. Hansen, P. F. Henry, H. E. Fischer, J. Torregrossa, and P. Convert, Meas. Sci. Technol. **19**, 034001 (2008).
[55] T. Kordel, D. Holland-Moritz, F. Yang, J. Peters, T. Unruh, T. Hansen, and A. Meyer, Phys. Rev. B **83**, 104205 (2011).
[56] P.-F. Paradis, T. Ishikawa, G.-W. Lee, D. Holland-Moritz, J. Brillo, W.-K. Rhim, and J. T. Okada, Mater. Sci. Eng., R **76**, 1 (2014).

[57] L. Hennet, D. Holland-Moritz, R. Weber, and A. Meyer, in *Neutron Scattering—Applications in Biology, Chemistry, and Materials Science*, Experimental Methods in the Physical Sciences, Vol. 49, edited by F. Fernandez-Alonso and D. L. Price (Academic Press, Cambridge, 2017), pp. 583–636.

[58] D. Holland-Moritz, T. Schenk, P. Convert, T. Hansen, and D. M. Herlach, Meas. Sci. Technol. **16**, 372 (2005).

[59] D. Holland-Moritz, S. Stüber, H. Hartmann, T. Unruh, T. Hansen, and A. Meyer, Phys. Rev. B **79**, 064204 (2009).

[60] J. Brillo, *Thermophysical Properties of Multicomponent Liquid Alloys* (De Gruyter, Oldenbourg, 2016).

[61] M. Schick, J. Brillo, I. Egry, and B. Hallstedt, J. Mater. Sci. **47**, 8145 (2012).

[62] D. B. Miracle, D. Louzguine-Luzgin, L. Louzguina-Luzgina, and A. Inoue, Int. Mater. Rev. **55**, 218 (2010).

[63] A. S. Clarke and J. D. Wiley, Phys. Rev. B **35**, 7350 (1987).

[64] D. Holland-Moritz, S. Stüber, H. Hartmann, T. Unruh, and A. Meyer, J. Phys.: Conf. Ser. **144**, 012119 (2009).

[65] V. F. Sears, Neutron News **3**, 26 (1992).

[66] S. P. Pan, J. Y. Qin, W. M. Wang, and T. K. Gu, Phys. Rev. B **84**, 092201 (2011).

[67] C. Wu, Y.-J. Huang, and J. Shen, Chin. Phys. Lett. **30**, 106102 (2013).

[68] M. D. Ediger, Annu. Rev. Phys. Chem **51**, 99 (2000).

[69] S. Sengupta, S. Karmakar, C. Dasgupta, and S. Sastry, J. Chem. Phys. **138**, 12A548 (2013).

[70] H. L. Peng and T. Voigtmann, Phys. Rev. E **94**, 042612 (2016).

[71] H. L. Peng, H. R. Schober, and T. Voigtmann, Phys. Rev. E **94**, 060601(R) (2016).

[72] B. Nowak, D. Holland-Moritz, F. Yang, Z. Evenson, and A. Meyer, Phys. Rev. B **97**, 094202 (2018).

[73] H. R. Schober, Solid State Commun. **119**, 73 (2001).

[74] L. Berthier and G. Biroli, Rev. Mod. Phys. **83**, 587 (2011).

[75] R. Yamamoto and A. Onuki, Phys. Rev. E **58**, 3515 (1998).

[76] S. Sengupta, S. Karmakar, C. Dasgupta, and S. Sastry, J. Chem. Phys. **140**, 224505 (2014).

[77] H. R. Schober and H. L. Peng, Phys. Rev. E **93**, 052607 (2016).

[78] A. Bartsch, K. Rätzke, A. Meyer, and F. Faupel, Phys. Rev. Lett. **104**, 195901 (2010).

[79] A. D. S. Parmar, S. Sengupta, and S. Sastry, Eur. Phys. J. E **41**, 90 (2018).

[80] T. Rizzo and T. Voigtmann, EPL **111**, 56008 (2015).

[81] T. Bryk and J.-F. Wax, Phys. Rev. B **80**, 184206 (2009).

[82] C. Kittel, *Introduction to Solid State Physics*, 8th ed. (John Wiley Sons, Hoboken, 2005).

[83] T. Bryk and I. Mryglod, J. Phys.: Condens. Matter **12**, 6063 (2000).

[84] T. Bryk, Eur. Phys. J. Special Topics **196**, 65 (2011).

[85] T. M. Bryk and I. M. Mryglod, Condens. Matter Phys. **10**, 481 (2007).

[86] T. Iwashita, D. M. Nicholson, and T. Egami, Phys. Rev. Lett. **110**, 205504 (2013).